epl A Letters Journal Exploring the Frontiers of Physics

March 2022

EPL, **137** (2022) 67001
doi: 10.1209/0295-5075/ac56ac

www.epljournal.org

Liquid demixing in elastic networks: Cavitation, permeation, or size selection?

Pierre Ronceray[1,2(a)], Sheng Mao[3,4], Andrej Košmrlj[4,5] and Mikko P. Haataja[4,5(b)]

[1] *Aix Marseille Univ, CNRS, CINAM, Turing Center for Living Systems - Marseille, France*
[2] *Center for the Physics of Biological Function, Princeton University - Princeton, NJ 08544, USA*
[3] *Department of Mechanics and Engineering Science, BIC-ESAT, College of Engineering, Peking University Beijing 100871, PRC*
[4] *Department of Mechanical and Aerospace Engineering, Princeton University - Princeton, NJ 08544, USA*
[5] *Princeton Institute of Materials, Princeton University - Princeton, NJ 08544, USA*

received 17 July 2021; accepted in final form 18 February 2022
published online 6 May 2022

Abstract – In cells, phase-separated liquid condensates interact mechanically with surrounding elastic networks such as chromatin and cytoskeleton. By considering the trade-offs between elastic, wetting, and interfacial energies, we theoretically show that three droplet phases can be thermodynamically stable: macroscopic droplets that either cavitate or permeate the network, and mesh-size–limited microdroplets. We show that network strain stiffening further enhances this latter size-limitation effect. Our theory predicts the possibility of yet-unobserved droplet phases in the cytoplasm and nucleoplasm.

Demixing of multicomponent biomolecular systems via liquid-liquid phase separation (LLPS) has emerged as a unifying mechanism governing the formation of many membrane-less intracellular bodies ("condensates") [1–6]. These droplets form in complex environments and often interact with elastic biopolymer networks, both in the cytoplasm (*e.g.*, stress granules and the cytoskeleton) and in the nucleoplasm (*e.g.*, nucleoli and chromatin). While both *in vivo* experiments [7] and studies of synthetic systems [8,9] demonstrate that such macromolecular networks strongly affect LLPS, a fundamental understanding of LLPS in an elastic network is still lacking.

In this letter we show that, upon accounting for capillary forces responsible for network expulsion, small-scale heterogeneity of the network, and its nonlinear mechanical properties, an intriguing picture of the thermodynamics of LLPS in elastic networks emerges. Specifically, we predict that, in addition to the experimentally observed cavitated droplets [7,8] which fully exclude the network, two new stable phases appear: elastically arrested, size-limited droplets at the network pore scale, and network-including macroscopic droplets. We argue that these phases may be relevant for intracellular condensates by rationalizing recent experimental observations of network inclusion [10,11], and predicting the possibility of pore size-limited condensates in chromatin.

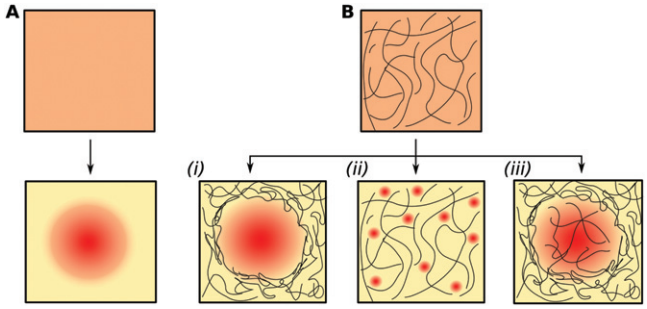

Fig. 1: (A) Classic liquid-liquid phase separation (LLPS) from an initially mixed phase (top) results in a macroscopic droplet of the minority phase (red) immersed in the yellow majority phase (bottom). (B) When LLPS occurs in the presence of an elastic network (top), three possible outcomes are considered (bottom): i) Cavitation. ii) Microdroplets. iii) Permeation of the network into the droplet.

When LLPS occurs without mechanical constraints (fig. 1(A)), interfacial energy considerations imply that the thermodynamically stable outcome is a macroscopic spherical droplet of the minority liquid (red) embedded within the majority phase (yellow), with an associated decrease in free energy per unit volume of $\Delta g_0 < 0$. In the presence of an elastic matrix hindering LLPS and

(a) E-mail: pierre.ronceray@univ-amu.fr
(b) E-mail: mhaataja@princeton.edu (corresponding author)

chemically distinct from the two liquids, in contrast, we consider three possible scenarios by which demixing can occur (fig. 1(B)). Each scenario results in a specific free energy cost compared to the reference, unhindered case: i) the minority liquid can create a macroscopic cavity, which incurs an elastic deformation energy penalty $E_{\rm el}$ associated with the network. ii) Alternatively, an extensive number of microdroplets may form within the pores of the network, which avoids elastic deformation but incurs an interfacial energy penalty $E_{\rm surf}$. iii) Finally, rather than fully excluding the network, the minority droplet can permeate through it, resulting in a wetting energy $E_{\rm wet}$. Below, we first introduce coarse-grained models that generically capture the physical features of LLPS in an elastic network and employ scaling arguments to evaluate the thermodynamic stability of each phase. To this aim, we assess the free energy penalty per droplet volume $\Delta g_{(i-iii)}$ incurred by the network in each scenario, compared to the reference case of a network-free infinite droplet: assuming that the network does not influence the composition and molar volume of the minority liquid, $\Delta g_{(i-iii)}$ is proportional to the chemical potential of the phase-separated liquid, and thus permits the identification of the most stable scenario. With this approach, we construct a phase diagram for the morphology of phase separation in an elastic network. We then develop a comprehensive theory of such systems based on the continuum mechanical modeling of the network, including finite compressiblity and nonlinear strain-stiffening effects. Analytical and numerical approaches are employed to both confirm the salient features of the phase diagram and elucidate the nature of phase transitions between the droplet phases.

We begin by considering scenario i), in which a macroscopic cavity of radius r forms from an initial pore. This scenario has been previously considered for *in vitro* oil-water mixtures in silicone gels [8,9,12] and *in vivo* droplets in the cell nucleus [7]. Within a neo-Hookean (NH) model for network elasticity [7–9], the elastic deformation energy $E_{\rm el}(r) \sim \frac{4\pi r^3}{3}\alpha G$ scales as the volume of the cavity in the limit $r \to \infty$. Here, G denotes the shear modulus of the network, while $\alpha \sim \frac{5}{2}$ is a material parameter (see sect. B in the Supplementary Material `Supplementarymaterial.pdf` (SM)). This simple behavior describes a broad class of artificial gels [13], while other mechanisms (*e.g.*, detachment of cross-links or fracture at fixed hoop stress [14,15]) can also lead to such a scaling. The free energy per droplet volume penalty is thus

$$\Delta g_{(i)} = \frac{3}{4\pi r^3} E_{\rm el}(r) \sim \alpha G. \tag{1}$$

We note that $\Delta g_{(i)}$ results in a shift of the demixing phase boundary to lower temperatures [8,16]. Remarkably, this behavior was validated for *in vitro* systems [8], with $\alpha \approx 1.5$. In the presence of macroscopic gradients in the network stiffness, (eq. (1)) also implies that droplet growth is favored in softer regions of the network [7,9,17,18].

While this model captures the macroscopic elastic response of the material, it does not account for small-scale heterogeneities. In both biological and artificial systems considered here, the elastic network is constituted by polymers with a finite pore/mesh size ξ. Consider now scenario ii) in fig. 1(B), in which microdroplets of radius $r \sim \xi$ form within these pores with negligible network deformation. In this case, $E_{\rm el} \approx 0$, while each microdroplet incurs an interfacial energy penalty $E_{\rm surf} \sim 4\pi\xi^2\gamma$, where γ denotes the surface tension between the two liquids. This results in a free energy per droplet volume penalty

$$\Delta g_{(ii)} \sim \frac{3\gamma}{\xi}. \tag{2}$$

Comparing eqs. (2) and (1) reveals that in such networks, the trade-off between elastic and interfacial energies is controlled by the *elasto-capillary number* [19]:

$$h \equiv \frac{3\gamma}{\xi G}. \tag{3}$$

When $h < \alpha$, *i.e.*, for large pore sizes and low liquid-liquid surface tensions, the thermodynamically stable phase thus corresponds to the formation of an extensive number of pore-size–limited microdroplets. In contrast, when $h > \alpha$, scenario i) is favored, with macroscopic cavitated droplets whose sizes are not constrained thermodynamically.

Finally, we consider scenario iii) from fig. 1(B): a macroscopic droplet encapsulating a partially excluded network. To assess its thermodynamic stability, we introduce a wetting energy $E_{\rm wet}$ via

$$E_{\rm wet} = \frac{4\pi r^3}{3}(1-\varphi)\sigma_p, \tag{4}$$

where φ denotes the fraction of network expelled from the droplet compared to the undeformed state, and σ_p is the *permeation stress*. Microscopically, σ_p arises from differential wetting energy per unit length of the filaments constituting the network in contact with the two fluids [20]. As further discussed in sect. E of the SM, a simple estimate for σ_p can be developed as follows. First, assume that the filaments comprising the network can be approximated as cylinders of radius r_f, corresponding to a liquid-solid interface area per unit length of $\sim 2\pi r_f$. Taking the filaments immersed in the majority liquid (liquid 1) as the reference point, the interfacial energy per unit length of a filament immersed in liquid 2 is thus $\sim 2\pi r_f(\gamma_{2S} - \gamma_{1S})$, where γ_{1S} and γ_{2S}, respectively, denote the interfacial energy between the filament and liquids 1 and 2. Denoting by ρ the volume fraction of the network in its undeformed state, the liquid-network contact area per unit volume is thus $\sim 2\rho/r_f$. Hence, the energy per unit volume difference between the network immersed in liquid 1 and in liquid 2 is $\sigma_p \sim 2\rho(\gamma_{2S} - \gamma_{1S})/r_f$. When $\sigma_p > 0$, the wetting energy of the filaments is lower in the majority liquid phase and filaments are repelled from the minority phase. In contrast, when $\sigma_p < 0$, it is lower in the minority liquid, and phase-separated droplets thus attract the surrounding network. Equation (4) translates this microscopic wetting

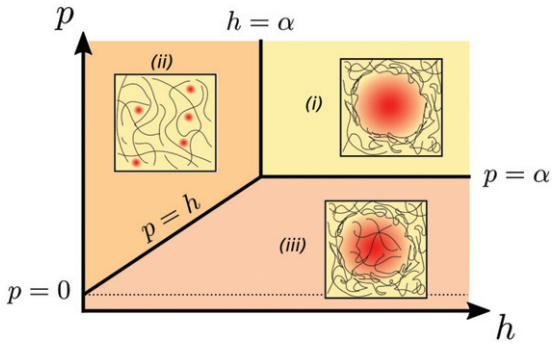

Fig. 2: Droplet phase diagram for LLPS in an elastic network constructed via scaling arguments. The most stable state is indicated in terms of the elasto-capillary h (eq. (3)) and the permeo-elastic p (eq. (6)) numbers. Note that only the dominant contribution to the free energy is retained here, corresponding to eqs. (1), (2) and (5), respectively, for the cavitated i), microdroplet ii), and permeated iii) phases.

phenomenon into a macroscopic effect, which results in a stress discontinuity at the liquid-liquid interface through which the network permeates. Network wetting may also induce an effective change of liquid-liquid surface tension, in particular if the filaments align with the interface; such effects are not considered in the present work.

To proceed with the analysis, we first ignore any σ_p-induced network deformations and set $\varphi = 0$. The free energy cost per volume induced by differential wetting is thus

$$\Delta g_{(iii)} \sim \sigma_p. \tag{5}$$

Comparing eqs. (5) and (1), we find that the thermodynamically stable phase is controlled by a second dimensionless quantity, namely the *permeo-elastic number*

$$p \equiv \frac{\sigma_p}{G}, \tag{6}$$

which is a measure of the degree of network deformation induced by the permeation stress. For $p > \alpha$, scenario i) is the most stable: the repulsion between the network and the minority liquid is sufficiently strong to fully expel the network from the droplet, leading to cavitation. For $p < \alpha$, the droplet permeates through the network rather than excluding it, and scenario iii) is preferred. Finally, when the elasto-capillary number $h < \alpha$, the phase boundary between scenarios ii) and iii) is given by the line $p = h$. The results of the scaling arguments are summarized in a phase diagram in the (p, h)-plane in fig. 2, which identifies the most stable droplet phase. For given material parameters (p, h), demixing will take place if $\Delta g_{\min} + \Delta g_0 < 0$, where $\Delta g_{\min} = \min[\Delta g_{(i)}, \Delta g_{(ii)}, \Delta g_{(iii)}]$. We note that for scenarios i), ii), the network hinders phase separation and stabilizes the mixed phase; for scenario iii), this depends on the sign of p: for $\sigma_p < 0$, the network prefers the minority phase and favors phase separation.

We have so far considered only the dominant contribution to the free energy for each scenario —either $E_{\rm el}$, $E_{\rm surf}$ or $E_{\rm wet}$. Network deformation, however, occurs in each of the three scenarios: in ii), microdroplets exert a pressure on the network, while in iii), a permeation stress $\sigma_p > 0$ results in a partial expulsion of the network from the droplet. To quantitatively predict the locations of the phase boundaries and the nature of associated phase transitions, we next discuss the deformation behavior arising from an isolated droplet embedded within a slightly compressible NH network characterized by a stored energy function $W = \frac{G}{2}\big[I_1 - 2(J-1) + \frac{(J-1)^2}{(1-2\nu)}\big]$. Here, $I_1 = \lambda_1^2 + \lambda_2^2 + \lambda_3^2$ and $J = \lambda_1\lambda_2\lambda_3$ with λ_k denoting the k-th principal stretch, while ν is the Poisson's ratio at small deformation [21].

Examining first scenarios i), ii) for which the network is fully excluded from the droplet, we consider a droplet of radius $r = \lambda_d \xi$ stretching a spherical cavity of initial radius ξ that corresponds to the characteristic pore size of the network (fig. 3(A)). The surface and elastic energy densities are $e_{\rm surf}(\lambda_d) = \frac{3\gamma}{\lambda_d \xi}$ and $e_{\rm el}(\lambda_d) = f_{\rm out}(\lambda_d) \equiv \frac{3}{\lambda_d^3} \min_{t(u)} \left[\int_1^\infty W\left(s(u), t(u), t(u)\right) u^2 {\rm d}u\right]$, with $s(u)$ and $t(u)$ denoting the radial and hoop stretches at distance $u\xi$ from the origin, subject to the boundary condition $t(1) = \lambda_d$ (see sects. A and B of the SM for derivation details and the perturbative calculation of $f_{\rm out}$). When the elasto-capillary number h is large (fig. 3(B)), $\Delta g = e_{\rm el} + e_{\rm surf}$ decreases monotonically with droplet size r, indicating that cavitation (scenario i) is thermodynamically favored. At small h (fig. 3(C)), in contrast, Δg exhibits a global minimum at $r^* \gtrsim \xi$, corresponding to size-limited microdroplets as per scenario ii). For positive Poisson's ratios ν, r^* increases sharply with the elasto-capillary number h (fig. 3(D)), but remains finite up to the limit of stability of microdroplets, indicating that the cavitation transition i) $\rightarrow$ ii) is weakly first order as surface tension is increased or, equivalently, as the shear modulus of the network is reduced. Interestingly, this transition becomes continuous for auxetic materials with $\nu < 0$ (see sect. C in the SM). We note that when scenario i) is favored, the total free energy of a droplet of size r presents a single maximum at the critical nucleation radius r_c, regardless of the value of Δg_0. This critical radius may be larger than the mesh size, in which case the nucleation rate is affected by the network. Nucleation and cavitation are thus concomitant in a single "nucleo-cavitation" step in NH materials, and mesh-size-level droplets are fully unstable, rather than being a metastable intermediate (except in a very narrow parameter regime; see SM).

Turning now to the case of a permeated network, we consider a macroscopic droplet (thus neglecting $e_{\rm surf}$) for which the wetting free energy per volume $e_{\rm wet}$ is a function of fraction $\varphi = 1 - \lambda_i^{-3}$ of the expelled network, where λ_i denotes the homogeneous stretch of the network inside the droplet (fig. 3(E)). In this case, $\Delta g = \min_{\lambda_i}\left[e_{\rm wet}(\lambda_i) + e_{\rm el}(\lambda_i)\right] = \min_{\lambda_i}\left[\frac{\sigma_p + W(\lambda_i,\lambda_i,\lambda_i)}{\lambda_i^3} + f_{\rm out}(\lambda_i)\right]$ (see sects. A and B in the SM). For large val-

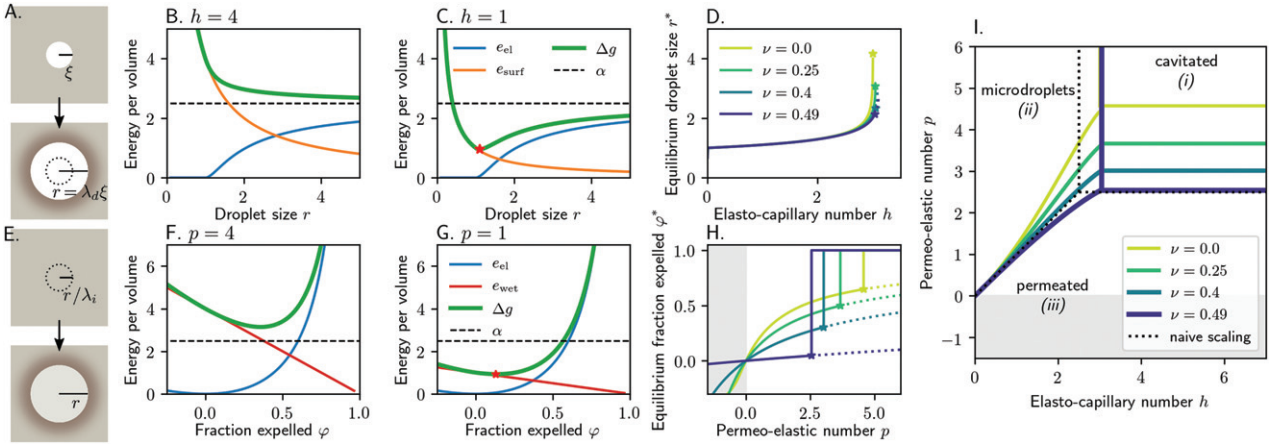

Fig. 3: Analysis of droplet phases within compressible neo-Hookean (NH) networks. (A) Sketch of the geometry of the pore deformation model. (B), (C): elastic energy (blue, $e_{\rm el}$), surface energy (orange, $e_{\rm surf}$) and total free energy (green, $\Delta g = e_{\rm el}+e_{\rm surf}$) per droplet volume *vs.* droplet size r, respectively for elasto-capillary numbers $h = 4$ (showing monotonic decay of Δg) and $h = 1$ (showing a global minimum of Δg at r^*, red star). Dashed black line indicates the $r \to \infty$ cavitated limit. (D) Equilibrium droplet size r^* *vs.* h, for different Poisson's ratios ν of the network. Star indicates the limit of stability of phase ii). (E) Sketch of the geometry for the permeation model with inner stretch λ_i. (F), (G): elastic energy, wetting energy (red, $e_{\rm wet}$) and total free energy (green, $\Delta g = e_{\rm el} + e_{\rm wet}$) per volume of a large droplet permeating through the network *vs.* fraction expelled of the network φ, respectively, for permeo-elastic numbers $p = 4$ (where cavitation is favored) and $p = 1$ (with global minimum at φ^*, red star). (H) Equilibrium fraction expelled φ^* *vs.* p. Dashed lines indicate metastable states, with cavitation ($\varphi^* = 1$) energetically favored. (I) Droplet phase diagram in the (p, h)-plane. Dotted lines indicate naive scaling results with $\alpha = 5/2$, as in fig. 2. The shaded area in (F), (G) indicate $p < 0$, *i.e.*, a contractile droplet attracting the network. In (A), (B), (D), (E) we take $\nu = 0.4$. Energy densities and length scales are normalized by the linear shear modulus G and the pore size ξ, respectively.

ues of p, Δg exceeds that of the cavitated case for all φ (fig. 3(F)). In contrast, at low p (fig. 3(G)), the global minimum of Δg occurs at $\varphi^* < 1$, and permeation is favored. When p increases, φ^* increases continuously up to the cavitation point, at which it experiences a compressibility-dependent jump (fig. 3(H)). We summarize these results in a phase diagram for NH materials in fig. 3(I).

While a NH constitutive law describes the deformation behavior of a broad class of materials at finite stretches, many biomolecular networks differ by exhibiting *strain-stiffening* behavior [22–24], whereby the (nominal) tensile stress grows faster than linearly with the stretch. In the permeated case, this nonlinearity limits the exclusion of the network from the droplet, with moderate effects on the phase stability. In contrast, strain stiffening strongly affects phases i) and ii) where the network is fully excluded: the free energy of the cavity grows asymptotically faster than its volume, and the elastic penalty $e_{\rm el}(r)$ diverges in the limit of large droplets, as illustrated in fig. 4(A) for a minimal model for power-law strain stiffening with an additional nonlinear contribution to stored energy function W given by $\frac{G}{2}[(I_1 - 3)/6\varepsilon_c]^3$. Here, the parameter ε_c controls the strength of the nonlinearity such that NH behavior is recovered in the limit $\varepsilon_c \to \infty$ (see sect. D in the SM). Thus, effectively $\alpha \to \infty$, and scenario i) is suppressed: the global energy minimum always occurs at a finite droplet radius r^*, leading to size selection [25]. When the nonlinearity is strong, the equilibrium droplet size $r^* \gtrsim \xi$ even at large capillary forces corresponding to $h \gg 1$ (fig. 4(B), blue), and microdroplets are stable

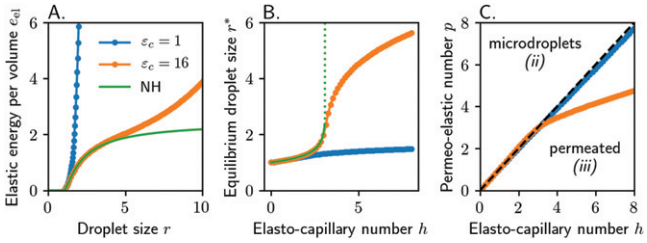

Fig. 4: Numerical analysis of networks with strong (blue) and weak (orange) strain stiffening behavior. The analytical solution for non-stiffening NH materials is also shown (green). (A) Elastic energy per droplet volume as a function of droplet size. (B) Equilibrium droplet size r^* as a function of the elasto-capillary number h. For NH materials, the cavitation transition is indicated by the dotted line. (C) Phase boundary between microdroplets ii) and permeated iii) phases. Cavitation i) is suppressed by the strain stiffening. Dashed line indicates the naive scaling $p = h$.

when $p \gtrsim h$ (fig. 4(C)). When the nonlinearity is weak and emerges only at large stretch, in contrast, microdroplets transition from being linearly arrested with size $r^* \gtrsim \xi$ at $h \lesssim 3$, to being non-linearly arrested at a mesoscopic size $r^* \gg \xi$ at $h \gtrsim 3$ (fig. 4, orange). This transition is a smooth crossover for realistic material parameters, and results in a change of slope of the phase boundary as larger droplets incur a lower surface penalty per unit volume (fig. 4(C)).

In summary, we have demonstrated that liquid-liquid phase separation (LLPS) in an elastic network dis-

Table 1: Order-of-magnitude estimates of the shear modulus G, network mesh size ξ, surface tension γ, and permeation stress σ_p for three classes of experimental systems. The ranges of variation of the elasto-capillary number h and the permeo-elastic number p are shown, and plausible scenarios for LLPS are indicated (most likely ones in bold). Details in sect. F in the SM.

System	G	ξ	γ	σ_p	h	p	Scenarios
I Oil in silicone gel	10^3–3.10^5 Pa	2–14 nm	4×10^3 Nm^{-1}	10^4–3.10^5 Pa	20–700	1.1–6.5	i), iii)
II Cytoplasmic cond.	10–100 Pa	50–150 nm	10^{-6} Nm^{-1}	$\pm$(0.2–2) Pa	0.2–6	$\pm(10^{-3}$–0.2)	ii), iii)
III Nuclear condensates	10–10^3 Pa	7–20 nm	10^{-7}–10^{-6} Nm^{-1}	$\pm$(10–100) Pa	0.01–10	$\pm$(0.01–10)	i), ii), iii)

plays complex morphological diversity at equilibrium. In particular, we have shown that the prevailing picture of cavitated macroscopic droplets is challenged by two alternative scenarios. On the one hand, when the pore-size-level elastic forces dominate the capillary forces, *i.e.*, when the elasto-capillary number h (eq. (3)) is small or when the network displays strong strain-stiffening behavior [25], stable pore-size–limited microdroplets form. We note that this equilibrium size limitation mechanism is distinct from previously considered kinetic limitation effects such as protocol-dependent arrested ripening of cavitated droplets [9,16,18,26] and hindered diffusion of irreversible nanoparticle aggregates in polymer gels [27]. On the other hand, when differential wetting between the network and the two liquids is not strong enough to fully expel the network, *i.e.*, for low permeo-elastic number p (eq. (6)), the network permeates the phase-separated droplets. Employing scaling arguments and continuum mechanics modeling that generically describe LLPS in an elastic network at a coarse-grained level (where the only parameters are the bulk material properties and the pore size), we have constructed a predictive morphological phase diagram that quantifies the equilibrium droplet size and network deformation behavior.

We note that our theoretical predictions rely on several important assumptions. First, we have focused on mechanical and thermodynamic equilibrium states, ignoring kinetic processes such as droplet nucleation [28], ripening [9,18,26] and merging [29], and, in the case of biological systems, their inherently out-of-equilibrium nature. Second, we have ignored all direct interactions between the droplets, which is justifiable when the typical droplet separations are much larger than their size. Third, we have neglected all visco-elastic effects in the network: we thus considered systems over time scales long enough for phase separation to complete, yet short enough for the network to retain its mechanical integrity.

We finally discuss the relevance of the predicted phase diagram for experimental systems by providing estimates for the relevant parameters, presented in table 1. For fluorinated oil demixing in silicone gels (system I with $h \gg \alpha$), consistent with experimental observations [8,9,12], only macroscopic phase separation appears to be relevant: these networks are too homogeneous, and the surface tension too high, to permit microphase separation. In contrast, for cytoplasmic condensates (system II), low surface tension, large mesh sizes and stiff filaments make permeation the most likely scenario, while cavitation appears to be ruled out by our theory: if droplets exclude the cytoskeleton, they are likely to be size selected at the network mesh size. In the context of intracellular phase separation in the nucleoplasm (III), all three scenarios are possible. In particular, DNA is only partially expelled from nucleoli [10], suggesting that these organelles may operate in the permeated regime with $p > 0$. Intriguingly, recent studies show that phase separation of HP1a leads to the formation of DNA-rich heterochromatin domains [11], suggesting a network-attracting permeated phase with $p < 0$. Finally, we predict that mesh-size–selected microdroplets are also possible in chromatin. Interestingly, the chromatin mesh size is well below the optical resolution limit: if such a phase exists, it may not have been fully characterized yet. For instance, it was recently proposed that phase-separated condensates are involved in the activation and repression of gene transcription [30–32]. Our work suggests that such condensates might be elastically limited by the mechanisms presented herein.

These order-of-magnitude estimates suggest that further super-resolution microscopy studies are needed to fully characterize intracellular LLPS, focusing both on the presence of network inclusion within membraneless condensates, and on the possible existence of elastically limited nanodroplets. We have also shown that existing synthetic systems for LLPS in elastic networks [8,9,12] operate in a parameter regime that is vastly different from intracellular LLPS (table 1). Our work provides design principles for new biomimetic systems which capture properties of *in vivo* systems more faithfully.

These engineered systems could be also useful for nanofabrication, as well as to serve as crucibles for chemical reactions favored by phase exchange: the very high surface-to-volume ratio would permit fast exchange between the two phases. The multi-stage chemical reactions can be guided in structured multi-phase droplets, such as is the case with the ribosome biogenesis in nucleoli [6], where the internal organization of phases is dictated by

their surface tensions [33]. Finally, our study underscores the importance of a novel quantity, the permeation stress σ_p, on LLPS. While we have focused on the case of droplets that (partially) expel the network, our theory predicts that capillary forces are reversed when $\sigma_p < 0$: in this case, the network facilitates phase separation and condenses around the droplets. Such network-droplet attraction could, *e.g.*, couple to the nonlinear mechanics of fiber networks to result in large-scale stresses [34,35], as well as yield new physical insights into the structure and function of biomolecular condensates.

* * *

SM is supported by Beijing Innovation Center for Engineering Science and Advanced Technology (BIC-ESAT) at Peking University. SM, AK and MPH are supported by NSF through the Princeton University Materials Research Science and Engineering Center DMR-2011750. MPH also acknowledges support from a Princeton University Focused Research Team award on Engineering Living Organelles. PR is supported by the NSF through the Center for the Physics of Biological Function (PHY-1734030), by the "Investissements d'Avenir" French Government program managed by the French National Research Agency (ANR-16-CONV-0001) and by the Excellence Initiative of Aix-Marseille University - A*MIDEX.

Data availability statement: All data that support the findings of this study are included within the article (and any supplementary files).

REFERENCES

[1] Brangwynne C. P., Eckmann C. R., Courson D. S., Rybarska A., Hoege C., Gharakhani J., Jülicher F. and Hyman A. A., *Science*, **324** (2009) 1729.
[2] Alberti S., Gladfelter A. and Mittag T., *Cell*, **176** (2019) 419.
[3] Hyman A. A., Weber C. A. and Jülicher F., *Annu. Rev. Cell Develop. Biol.*, **30** (2014) 39.
[4] Berry J., Brangwynne C. P. and Haataja M., *Rep. Prog. Phys.*, **81** (2018) 046601.
[5] Choi J.-M., Holehouse A. S. and Pappu R. V., *Annu. Rev. Biophys.*, **49** (2020) 107.
[6] Feric M., Vaidya N., Harmon T. S., Mitrea D. M., Zhu L., Richardson T. M., Kriwacki R. W., Pappu R. V. and Brangwynne C. P., *Cell*, **165** (2016) 1686.
[7] Shin Y., Chang Y.-C., Lee D. S. W., Berry J., Sanders D. W., Ronceray P., Wingreen N. S., Haataja M. and Brangwynne C. P., *Cell*, **175** (2018) 1481.
[8] Style R. W., Sai T., Fanelli N., Ijavi M., Smith-Mannschott K., Xu Q., Wilen L. A. and Dufresne E. R., *Phys. Rev. X*, **8** (2018) 011028.
[9] Rosowski K. A., Sai T., Vidal-Henriquez E., Zwicker D., Style R. W. and Dufresne E. R., *Nat. Phys.*, **16** (2020) 422.
[10] Sluis M. v., Vuuren C. v., Mangan H. and McStay B., *Proc. Natl. Acad. Sci. U.S.A.*, **117** (2020) 10368.
[11] Strom A. R., Emelyanov A. V., Mir M., Fyodorov D. V., Darzacq X. and Karpen G. H., *Nature*, **547** (2017) 241.
[12] Kim J. Y., Liu Z., Weon B. M., Cohen T., Hui C.-Y., Dufresne E. R. and Style R. W., *Sci. Adv.*, **6** (2020) eaaz0418.
[13] Treloar L. R. G., The Physics of Rubber Elasticity, third edition, *Edition Oxford Classic Texts in the Physical Sciences* (Oxford University Press, Oxford, NY) 2005.
[14] Raayai-Ardakani S., Earl D. R. and Cohen T., *Soft Matter*, **15** (2019) 4999.
[15] Vidal-Henriquez E. and Zwicker D., *Proc. Natl. Acad. Sci. U.S.A.*, **118** (2021) e2102014118.
[16] Kothari M. and Cohen T., *J. Mech. Phys. Solids*, **145** (2020) 104153.
[17] Vidal-Henriquez E. and Zwicker D., *Soft Matter*, **16** (2020) 5898.
[18] Rosowski K., Vidal-Henriquez E., Zwicker D., Style R. W. and Dufresne E. R., *Soft Matter*, **16** (2020) 5892.
[19] Shao X., Fredericks S. A., Saylor J. R. and Bostwick J. B., *Phys. Rev. Lett.*, **123** (2019) 188002.
[20] De Gennes P. G., *J. Phys. Chem.*, **88** (1984) 6469.
[21] Biwa S., *Int. J. Non-Linear Mech.*, **41** (2006) 1084.
[22] Ogden R. W., *Non-linear Elastic Deformations* (Courier Corporation) 1997.
[23] Storm C., Pastore J. J., MacKintosh F. C., Lubensky T. C. and Janmey P. A., *Nature*, **435** (2005) 191.
[24] Erk K. A., Henderson K. J. and Shull K. R., *Biomacromolecules*, **11** (2010) 1358.
[25] Wei X., Zhou J., Wang Y. and Meng F., *Phys. Rev. Lett.*, **125** (2020) 268001.
[26] Zhang Y., Lee D. S. W., Meir Y., Brangwynne C. P. and Wingreen N. S., *Phys. Rev. Lett.*, **126** (2021) 258102.
[27] Laxton P. B. and Berg J. C., *Langmuir*, **24** (2008) 9268.
[28] Shimobayashi S. F., Ronceray P., Sanders D. W., Haataja M. P. and Brangwynne C. P., *Nature*, **599** (2021) 503.
[29] Lee D. S. W., Wingreen N. S. and Brangwynne C. P., *Nat. Phys.*, **17** (2021) 531.
[30] Cho W.-K., Spille J.-H., Hecht M., Lee C., Li C., Grube V. and Cisse I. I., *Science*, **361** (2018) 412.
[31] Sabari B. R., Dall'Agnese A., Boija A., Klein I. A., Coffey E. L., Shrinivas K., Abraham B. J., Hannett N. M., Zamudio A. V., Manteiga J. C., Li C. H., Guo Y. E., Day D. S., Schuijers J., Vasile E., Malik S., Hnisz D., Lee T. I., Cisse I. I., Roeder R. G., Sharp P. A., Chakraborty A. K. and Young R. A., *Science*, **361** (2018) eaar3958.
[32] Treen N., Shimobayashi S. F., Eeftens J. *et al.*, *Nat. Commun.*, **12** (2021) 1561.
[33] Mao S., Chakraverti-Wuerthwein M. S., Gaudio H. and Košmrlj A., *Phys. Rev. Lett.*, **125** (2020) 218003.
[34] Ronceray P., Broedersz C. P. and Lenz M., *Proc. Nat. Acad. Sci. U.S.A.*, **113** (2016) 2827.
[35] Ronceray P., P. Broedersz C. and Lenz M., *Soft Matter*, **15** (2019) 331.

Liquid demixing in elastic networks: cavitation, permeation, or size selection? Supplementary Information

Appendix A: Mathematical framework: modeling liquid droplets in an elastic network

We first discuss the framework we employ to assess the stability of each of the three scenarios considered in the main text: *(i)* cavitation, *(ii)* microdroplets, and *(iii)* permeation. Throughout this article, we consider a single spherical droplet of phase-separated liquid, in an infinite elastic medium representing the network. We thus neglect mechanical interactions between droplets, mediated by the network; this assumption is valid if the separation between droplets is much larger than their size (*i.e.* when the volume fraction of phase-separated droplets is small). The stability of each scenario is measured by the difference Δg of free energy per droplet volume, compared to an infinite droplet of phase separated liquid in the absence of an elastic network. This penalty is captured in three distinct terms: elastic energy stored in the network, liquid-liquid surface tension, and wetting energy. The latter two have closed forms as a function of the droplet size and inner stretch. The mathematically non-trivial aspect thus lies in the evaluation of the elastic energy resulting from the network deformation induced by the droplet.

We characterize the elastic medium by its *stored energy function* $W(\lambda_1, \lambda_2, \lambda_3)$ (which we leave unspecified for now), where the λ_i's correspond to the three principal stretches. This function corresponds to the elastic energy density in the undeformed material coordinates. We consider a droplet of size r_d in a spherically symmetric infinite medium. We write the equilibrium deformation $r = r(R)$, such that a point at distance R from the droplet center in the initial undeformed state is displaced to radius $r(R)$ in the deformed state. In this geometry, the principal stretches are the radial stretch $\lambda_1(R) = \frac{dr}{dR} \equiv s$ and the hoop stretch $\lambda_2(R) = \lambda_3(R) = r/R \equiv t$.

We distinguish two geometries, depending on whether the network is excluded from the droplet (scenarios *(i-ii)*) or included (scenario *(iii)*):

- excluded network (Fig. 1A): the medium is modeled as an infinite material with an initial spherical pore of radius ξ in the reference configuration (left). A droplet of radius $r_d = r(\xi)$ stretches this pore by a factor $\lambda_d = r_d/\xi$ compared to this reference configuration (right). The elastic energy stored in the network outside the droplet is thus:

$$E_{\text{el,out}} = 4\pi \int_{\xi}^{\infty} W\left(\frac{dr}{dR}, \frac{r}{R}, \frac{r}{R}\right) R^2 dR \tag{A1}$$

  Introducing $u = R/\xi$, the radial stretch $s = dr/dR$ and the hoop stretch $t = r/R$, we obtain the following form for the elastic energy per unit volume of the droplet:

$$\frac{E_{\text{el,out}}}{v_d} = \frac{3}{\lambda_d^3} \int_1^{\infty} W\left(s(u), t(u), t(u)\right) u^2 du \equiv f_{\text{out}}(\lambda_d) \tag{A2}$$

  where $v_d = \frac{4}{3}\pi r_d^3$ is the droplet volume. Eq. (A2) should be minimized over the deformation field $t(u)$, with boundary condition $t(u = 1) = \lambda_d$.

- included (permeated) network (Fig. 1B): the medium is modeled as an intact infinite material, and the pores are considered to be infinitesimally small. The droplet of radius r_d is placed at the center, and imposes a stress discontinuity at its surface. The material inside the droplet is isotropically and homogeneously deformed with stretch λ_i. The material outside the droplet is deformed in a similar way as previously, and hence the total elastic energy reads

$$E_{\text{el}} = E_{\text{el,in}} + E_{\text{el,out}} = \frac{4}{3}\pi \left(\frac{r_d}{\lambda_i}\right)^3 W(\lambda_i, \lambda_i, \lambda_i) + 4\pi \int_{r_d/\lambda_i}^{\infty} W\left(\frac{dr}{dR}, \frac{r}{R}, \frac{r}{R}\right) R^2 dR \tag{A3}$$

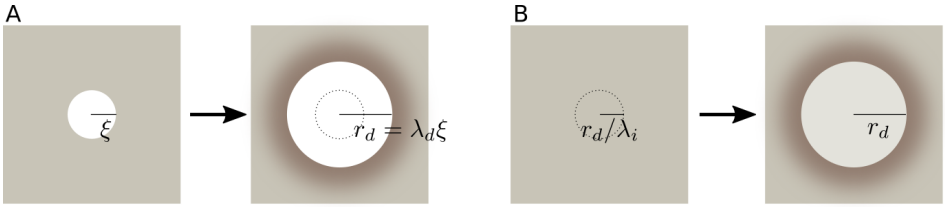

FIG. 1. Geometries of droplets considered here. **A.** Network exclusion, starting from a pore of size ξ stretched by a factor λ_d. **B.** Permeation of the droplet through the network, with network stretch λ_i inside the droplet.

which, divided by the droplet volume, is:

$$\frac{E_{\rm el}}{v_d} = \frac{1}{\lambda_i^3} W(\lambda_i, \lambda_i, \lambda_i) + f_{\rm out}(\lambda_i) \tag{A4}$$

where $f_{\rm out}$ was defined in Eq. (A2). In this geometry, the fraction of the network excluded from the droplet is $\varphi = 1 - \lambda_i^{-3}$, so that the wetting energy reads $E_{\rm wet} = v_d \sigma_p \lambda_i^{-3}$.

We finally recapitulate our definition of the free energy for each of the three phases considered in this article.

- Cavitation *(i)*: the only contribution to the free energy is the elastic penalty, in the infinite-stretch limit of Eq. (A2):

$$\Delta g_{(i)} = \lim_{\lambda_d \to \infty} f_{\rm out}(\lambda_d). \tag{A5}$$

- Microdroplets *(ii)*: we combine the elastic energy with network exclusion (Eq. (A2)) with the surface tension. The free energy is found by minimizing over the pore stretch (*i.e.* over the droplet radius):

$$\Delta g_{(ii)} = \min_{\lambda_d} \left[\frac{3\gamma}{\lambda_d \xi} + f_{\rm out}(\lambda_d) \right] \tag{A6}$$

where γ is the surface tension. Note that the minimization does not always yield a finite value for λ_d.

- Permeation *(iii)*: we combine the elastic energy with network inclusion (Eq. (A4)) with the wetting energy. The free energy is found by minimizing over the pore stretch (*i.e.* over the excluded fraction of the network):

$$\Delta g_{(iii)} = \min_{\lambda_i} \left[\frac{\sigma_p + W(\lambda_i, \lambda_i, \lambda_i)}{\lambda_i^3} + f_{\rm out}(\lambda_i) \right] \tag{A7}$$

where σ_p is the permeation stress.

The mathematically non-trivial part, in all three scenarios, is the evaluation of the outer elastic energy density $f_{\rm out}(\lambda)$. We combine two approaches, depending on the class of materials considered, *i.e.* on the functional form of W. In the case of neo-Hookean materials, we consider slightly compressible systems, which allows us to solve for the deformation field analytically, as discussed in Sec. B (corresponding to the results presented in Fig. 3 of the main text). For strain-stiffening materials (Fig. 4 of the main text), such an analytical approach is not possible, and we resort to a numerical estimation of $f_{\rm out}$, as presented in Sec. D. In all cases, the free energy minimization over the value of λ in Eqs. (A6) and (A7) is then performed numerically.

Appendix B: Analytical treatment of slightly compressible neo-Hookean materials

Consider Eq. (A1), written in terms of arbitrary inner and outer radii R_{min} and R_{max}: $E_{\rm el,out} = \int_{R_{min}}^{R_{max}} 4\pi R^2 W(\lambda_1, \lambda_2, \lambda_2) dR$. In mechanical equilibrium, $E_{\rm el,out}$ is a minimum. Thus, the equilibrium deformation $r = r(R)$ can be obtained from a variational principle as

$$\frac{\delta E_{\rm el,out}}{\delta r(R)} = 8\pi R \frac{\partial W}{\partial \lambda_2} - 4\pi \frac{d}{dR}\left(R^2 \frac{\partial W}{\partial \lambda_1} \right) = 0, \tag{B1}$$

or

$$\frac{d}{dR}\left(R^2 W_1\right) - 2R W_2 = 0, \tag{B2}$$

where $W_i \equiv \partial W / \partial \lambda_i$. [Note that here we assume that the system is compressible. In an incompressible system, the deformation is explicitly determined from $J = \frac{dr}{dR}\left(\frac{r}{R}\right)^2 = 1 \leftrightarrow \frac{dr}{dR} = \left(\frac{r}{R}\right)^{-2}$.] It is straightforward to show that $dW_1/dR = W_{11} r''(R) + 2W_{12}(r'(R)/R - r/R^2)$, where $W_{1j} \equiv \partial^2 W / \partial \lambda_1 \partial \lambda_j$. Upon introducing the hoop and radial stretches as $t = r(R)/R$ and $s(t) = dr/dR$, respectively, it can be shown that $r''(R) = ds/dR = ds/dt\,(s-t)/R$ and $dW_1/dR = W_{11}[ds/dt\,(s-t)/R] + 2W_{12}[s-t]/R$. Thus, Eq. (B2) becomes

$$W_{11} \frac{ds}{dt} = -2\left(\frac{W_1 - W_2}{s - t} + W_{12} \right). \tag{B3}$$

Let us next focus on the following simple form for the stored energy function W, corresponding to a slightly compressible neo-Hookean network [1]:

$$W(\lambda_1,\lambda_2,\lambda_3)=\frac{G}{2}\left[\lambda_1^2+\lambda_2^2+\lambda_3^2-3-2(\lambda_1\lambda_2\lambda_3-1)+\beta\left(\lambda_1\lambda_2\lambda_3-1\right)^2\right], \tag{B4}$$

with G and $\nu=(1-\beta^{-1})/2$ denoting the shear modulus and Poisson's ratio, respectively. It is straightforward to show that, with this choice for W, Eq. (B3) becomes

$$\left(1+\beta t^4\right)\frac{ds}{dt}=-2\left(1+\beta s t^3\right). \tag{B5}$$

The exact solution of Eq. (B5) is given by [1]

$$s(t)=\frac{C_0-\Psi(t)}{\sqrt{1+\beta t^4}}, \tag{B6}$$

where C_0 denotes an integration constant, and

$$\frac{d\Psi(t)}{dt}=\frac{2}{\sqrt{1+\beta t^4}}\quad\leftrightarrow\quad\Psi(t)=\int_{t_0}^{t}d\tau\frac{2}{\sqrt{1+\beta\tau^4}}. \tag{B7}$$

Now, consider the case where we have an initial pore of radius ξ embedded within an infinite elastic, neo-Hookean matrix, and the pore walls are subjected to a constant pressure p_0. Far from the cavity, the matrix remains deformation-free, and hence $\lim_{t\to1}s(t)=1$. From the exact solution we immediately obtain

$$s_I(t)=\frac{\sqrt{1+\beta}-\int_1^t d\tau\frac{2}{\sqrt{1+\beta\tau^4}}}{\sqrt{1+\beta t^4}}. \tag{B8}$$

Now, consider subjecting the boundary of the pore to a stretch λ such that $r(\xi)=\lambda\xi$. The corresponding radial stretch is given by

$$s_I(\lambda)\equiv\Delta_I=\frac{\sqrt{1+\beta}-\int_1^\lambda d\tau\frac{2}{\sqrt{1+\beta\tau^4}}}{\sqrt{1+\beta\lambda^4}}. \tag{B9}$$

Now, the pressure p_0 required to sustain the deformation is given by

$$\frac{p_0(\lambda,\beta)}{G}=-\frac{W_1}{G\lambda^2}=1-\frac{\Delta_I}{\lambda^2}-\beta\left(\Delta_I\lambda^2-1\right). \tag{B10}$$

We obtain the stored elastic energy as the total work of pressure forces from the undeformed state:

$$E_{\mathrm{el,out}}(\lambda)=4\pi\xi^3\int_1^\lambda p_0(\lambda',\beta)\lambda'^2d\lambda' \tag{B11}$$

Using the formal calculus software SymPy [2] to expand the integral in Eq. (B9) in powers of β^{-1} (*i.e.* a weakly compressible expansion), we finally obtain the following expression for the elastic energy per droplet volume f_{out} as a function of the droplet stretch $\lambda=r/\xi$:

$$\begin{aligned}\frac{f_{\mathrm{out}}(\lambda)}{G}=&+\frac{5}{2}-\frac{3}{\lambda}-\frac{1}{\lambda^3}+\frac{3}{2\lambda^4}\\&+\beta^{-1}\left[-\frac{3}{40}+\frac{6}{5\lambda^3}-\frac{9}{4\lambda^4}+\frac{6}{5\lambda^5}-\frac{3}{40\lambda^8}\right]\\&+\beta^{-2}\left[\frac{1}{48}-\frac{2}{15\lambda^3}+\frac{9}{80\lambda^4}+\frac{9}{80\lambda^8}-\frac{2}{15\lambda^9}+\frac{1}{48\lambda^{12}}\right]\\&+\beta^{-3}\left[-\frac{15}{1664}+\frac{14}{325\lambda^3}-\frac{1}{32\lambda^4}-\frac{9}{1600\lambda^8}-\frac{1}{32\lambda^{12}}+\frac{14}{325\lambda^{13}}-\frac{15}{1664\lambda^{16}}\right]\\&+\beta^{-4}\left[\frac{21}{4352}-\frac{22}{1105\lambda^3}+\frac{45}{3328\lambda^4}+\frac{1}{640\lambda^8}+\frac{1}{640\lambda^{12}}+\frac{45}{3328\lambda^{16}}-\frac{22}{1105\lambda^{17}}+\frac{21}{4352\lambda^{20}}\right]\\&+\beta^{-5}\left[-\frac{3}{1024}+\frac{22}{1989\lambda^3}-\frac{63}{8704\lambda^4}-\frac{9}{13312\lambda^8}-\frac{1}{2304\lambda^{12}}-\frac{9}{13312\lambda^{16}}-\frac{63}{8704\lambda^{20}}+\frac{22}{1989\lambda^{21}}-\frac{3}{1024\lambda^{24}}\right]\\&+O\left(\beta^{-6}\right)\end{aligned} \tag{B12}$$

which we use to assess the stability of each phase, as described in Sec. A. For $\nu > 0$ (corresponding to $\beta > 1$ this expansion converges rapidly, and the results are essentially unaffected by including additional terms (in practice, for the results presented in Fig. 3 of the main text, we expand up to β^{-8}). In particular, we can read out the $\lambda \to \infty$ limit, corresponding to the cavitated free energy (Eq. (A5)):

$$\alpha \equiv \frac{\Delta g_{(i)}}{G} = \frac{1}{G}\lim_{\lambda\to\infty} f_{\text{out}}(\lambda) = \frac{5}{2} - \frac{3}{40\beta} + \frac{1}{48\beta^2} - \frac{15}{1664\beta^3} + \frac{21}{4352\beta^4} - \frac{3}{1024\beta^5} + \frac{99}{51200\beta^6} + O\left(\beta^{-7}\right) \tag{B13}$$

Note that we also have $\alpha = p_0^*/G$, where p_0^* is the cavitation pressure. As expected, in the limit $\beta \to \infty$, $p_0^*/G \to 5/2$, in agreement with the classic cavitation result for incompressible neo-Hookean materials. For reasonable values of $\nu = 1/3$ ($\beta = 3$) or $\nu = 1/4$ ($\beta = 2$), Eq. (B13) yields $p_0^*/G \approx 2.48$ and 2.47, respectively. Finite compressibility thus reduces the critical cavitation pressure, albeit to a rather small degree. We also note that for the special case $\beta = 1$ (corresponding to $\nu = 0$), $p_0^*/G = 2 - \sqrt{2} + 4/\sqrt{\pi}\ \Gamma^2(5/4) \approx 2.44$, where $\Gamma(x)$ denotes the Euler gamma function, while the series approximation in Eq. (B13) yields $p_0^*/G \approx 2.44$, in excellent agreement with the exact result. Cavitation pressures for several representative compressibilities are listed in **Table 1**.

β	1	2	3	5	10	50	∞
ν	0	1/4	1/3	0.4	0.45	0.49	1/2
$\alpha = p_0^*(\beta)/G$	2.439	2.467	2.477	2.486	2.493	2.4985	5/2

TABLE I. Critical cavitation pressure of a finite spherical pore in an infinite, slightly compressible Neo-Hookean matrix at varying compressibilities.

Appendix C: Limit of metastability of microdroplets in the neo-Hookean model

We investigate here the nature of the equilibrium transition between microdroplets (scenario *ii*) and cavitation (scenario *i*), which is controlled by the elasto-capillary number h. To this aim, it is useful to consider the free energy per volume of a droplet of size $r = \lambda\xi$ as a function of its stretch λ, in the large λ limit that can be read out from Eq. (B12):

$$\frac{1}{G}\Delta g(\lambda) = \alpha(\beta) + \frac{h-3}{\lambda} + \frac{A_3(\beta)}{\lambda^3} + O(\lambda^{-4}) \tag{C1}$$

where again $\beta = 1/(1-2\nu)$ is the compressibility parameter, and $A_3(\beta)$ is the coefficient of the inverse cubic term. Interestingly, the leading order in the expansion changes sign when $h = 3$ (independently of β), and around this value the free energy is thus dominated by higher-order terms. Depending on the compressibility, we identify two qualitatively distinct behaviors when varying h, as shown in Fig. 2:

- for $\nu > 0$, *i.e.* for usual materials, we have the following sequence of regimes:
  - $h < 3$: $\Delta g(\lambda)$ exhibits a single minimum at a finite $\lambda^* = r^*/\xi$, corresponding to the microdroplets scenario. Near equilibrium, droplets larger than r^* would shrink ("anti-ripen") so as to reach the equilibrium size.
  - $3 < h < h_c$: microdroplets are the global free energy minimum, but there is a local maximum at $\lambda > \lambda^*$. As a result, $\lambda = \infty$ is a local minimum of free energy, and cavitated droplets are metastable.
  - $h_c < h < h^\dagger$: the global minimum of free energy is at $\lambda = \infty$, and cavitation is the stable scenario; however, a local minimum exists at $r^\dagger$, corresponding to metastable microdroplets.
  - $h > h^\dagger$: the free energy is monotonically decreasing as a function of λ, cavitation is stable and there exists no metastable state.

  The transition between scenarios (*i*) and (*ii*) governed by h is thus first-order. However, plotting in Fig. 3 the values of h_c and $h^\dagger$ over the physical range of Poisson's ratio values ν, we note that the range of metastability corresponding to this first-order transition is very narrow, and restricted to values $3 < h < 3.11$ for all ν.
- for $\nu < 0$, *i.e.* for auxetic materials, we observe a second-order transition between scenarios *(i)* and *(ii)* (right panels in Fig. 2), with a continuous divergence of the droplet radius as $r^* \sim (3-h)^{-1/2}$ as $h \to 3$.

Overall, this analysis shows that at $\nu > 0$ the cavitation transition is *weakly first order*, characterized by the proximity to a critical point at $\nu = 0$, sharp increase of the droplet size near the transition (as shown in Fig 3C of the main text), and very limited range of metastability.

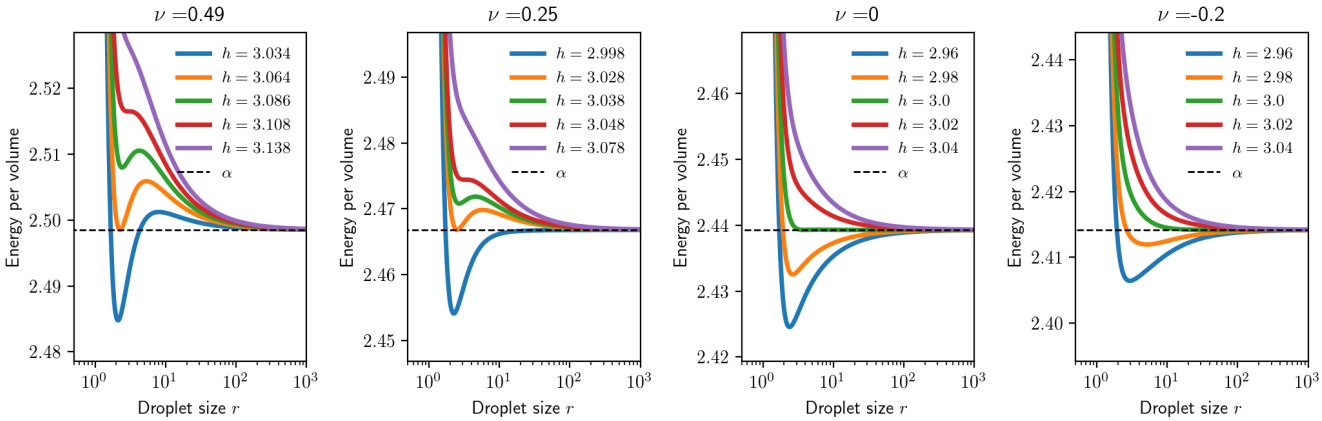

FIG. 2. Plots of $\frac{1}{G}\Delta g(\lambda)$ for different values of h and ν. The metastability regimes corresponding to a first-order transition are apparent for $\nu > 0$ (left two panels, with the equilibrium transition $h = h_c$ in orange and the end of metastability $h = h^\dagger$ in red). For $\nu \leq 0$ (right two panels), the transition is second-order and occurs at $h = 3$.

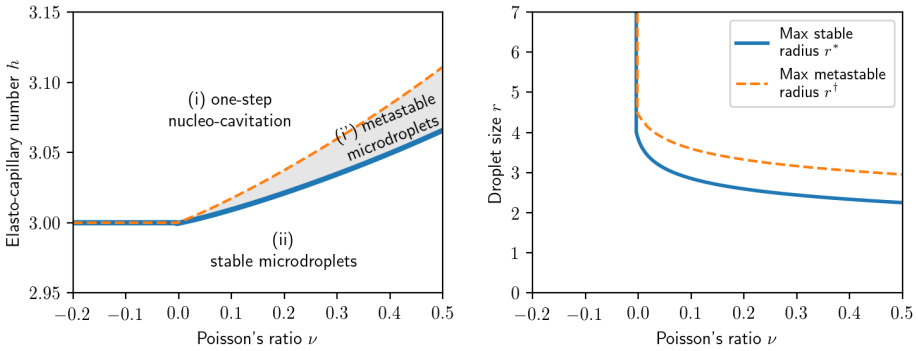

FIG. 3. Left: equilibrium transition line h_c (solid blue line) and metastability limit $h^\dagger$ (dashed orange line) as a function of Poisson's ratio ν. The shaded area indicates the region in which microdroplets can be metastable. Note the very limited range of h values represented here. Right: maximum radius for stable microdroplets (solid blue line) and metastable droplets (dashed orange line). At $\nu < 0$ these are infinite, as the cavitation transition is continuous.

Appendix D: Minimal model for strain-stiffening effects

The stored energy function W for neo-Hookean materials [3] in Eq. (B4) does not capture strain-stiffening effects occuring in macromolecular systems at large stretches [4–8]. To account for such effects, we consider the following modified stored energy function:

$$W = \frac{G}{2}\left[(I_1 - 3) - 2(J-1) + \beta(J-1)^2 + \left(\frac{I_1 - 3}{6\,\varepsilon_c}\right)^3\right], \tag{D1}$$

where $I_1 = \lambda_1^2 + \lambda_2^2 + \lambda_3^2$ and $J = \lambda_1\lambda_2\lambda_3$, and where ε_c denotes a characteristic strain at which stiffening effects become significant. It should be noted that the last term in Eq. (D1) emerges as the leading order term in a polynomial expansion of the classic Arruda-Boyce [7, 8] and Gent [6] models for large-stretch behavior of polymer systems.

The above choice for W is both convenient and physically-based: (1) At infinitesimally small strains, $W \sim G\left[\epsilon_{ij}\epsilon_{ij} + \frac{\nu}{1-2\nu}\epsilon_{ii}\epsilon_{jj}\right]$, in accordance with linear elasticity theory, where $\beta^{-1} = (1-2\nu)$ with ν denoting the Poisson's ratio and $\boldsymbol{\epsilon}$ the linear strain. (2) By taking $\varepsilon_c \to \infty$, we recover the (slightly) compressible neo-Hookean model in Eq. (B4). (3) Asymptotically, $W \sim [(I_1-3)/(6\varepsilon_c)]^3 \sim \left[(\lambda^2_{chain} - 1)/(2\varepsilon_c)\right]^3$, indicating a strong stiffening effect when $I_1 \to (3+6\varepsilon_c)$. Therefore, this form of W can be viewed as a minimal model for slightly compressible, strain-stiffening hyperelastic materials. Specifically, by tuning the parameter β, we can vary the compressibility with $\beta \to \infty$ corre-

sponding to a perfectly incompressible material, while by tuning ε_c, we can vary the material response from weakly stiffening (large ε_c) to strongly stiffening (small ε_c).

We employ numerical simulations to study the influence of strain-stiffening of the network on liquid-liquid phase separation. Specifically, to evaluate $f_{\rm out}(\lambda)$ (as given by Eq. (A2)), we discretize the displacement field over an uneven grid, $u = [1, 1.16, 1.33, 1.51, ..., 28.4, 29.2, u_{\rm max} = 30]$ (with regular spacing of the values of $\sqrt{u}$). We evaluate the integral $\int_1^{u_{\rm max}} W\left(s(u), t(u), t(u)\right) u^2 du$ using finite differences of the displacement field, and use the SciPy optimization package [9] (`scipy.optimize.minimize`) to perform the multivariate minimization of the energy of the displacement field, under the constraint $r(u = 1) = \lambda$. The outcome of this optimization is insensitive to the details of the discretization, and recovers the analytical solution presented in Sec. B in the case of neo-Hookean materials. We then pipe the resulting function $f_{\rm out}(\lambda)$ into the free energy minimization described in Eqs. (A6)-(A7).

Appendix E: Further discussion of permeation stress σ_p.

We now provide further insights into the permeation stress σ_p, and discuss how it could be measured in practice. First, recall from the main text the expression for σ_p:

$$\sigma_p \sim \frac{2}{r_f}\rho(\gamma_{2S} - \gamma_{1S}), \tag{E1}$$

where r_f, ρ, and γ_{1S} (γ_{2S}) denote the filament radius, network volume fraction, and interfacial energy between the filament and liquid 1 (2). In the presence of strain in the network, its volume fraction may change: denoting by $\varphi = 1 - 1/(\lambda_1\lambda_2\lambda_3)$ the fraction of the network that is expelled compared to the undeformed state (where the λ_i's are principal stretches), the energy per volume associated with immersing the stretched network into the minority liquid is thus $(1-\varphi)\sigma_p$, corresponding to Eq. 5 of the main text.

At the liquid-liquid interface, the difference in surface energy results in a capillary force $F_c \sim 2\pi r_f(\gamma_{2S} - \gamma_{1S})$ on each filament going through the interface. At the network scale, this implies a stress discontinuity in the network: the network is being "sucked in" by the best-wetting liquid. Note that while Eq. (E1) relies on microscopic modeling of the network and applicability of the surface energy at the level of individual filaments, this stress discontinuity suggests that σ_p could also be measured experimentally, in a way that is independent from microscopic models. Indeed, consider a tube separating two chambers containing respectively liquids 1 and 2, with a cork of clamped network in the tube. Then σ_p corresponds to the pressure difference one must impose between the two chambers, so that the liquid-liquid interface remains steady within the network cork. This provides an experimentally viable way to measure σ_p. The existence and microscopic origin of this term was previously noted by de Gennes in the context of non-deformable porous media [10].

Note that in addition to the difference of liquid-solid surface energy, it is possible that the rest state of the network changes when immersed in liquid 2 – either swelling or shrinking – and thus that permeation induces a spontaneous strain in the network. This qualitatively distinct effect has, in practice, consequences similar to the effect discussed above, and thus simply results in a modification of σ_p for our purposes. Finally, network wetting may also induce an effective change of liquid-liquid surface tension, in particular if the filaments align with the interface; such effects are not considered in the present work.

Appendix F: Estimation of physical parameters.

Here we discuss how we obtain the experimental values of parameters presented in Table I of the main text, for each of the three classes of systems considered. We focus on obtaining order-of-magnitude estimates for the two dimensionless parameters introduced in the main text: the elasto-capillary number $h \equiv 3\gamma/\xi G$ with γ the liquid-liquid surface tension, ξ the network pore size, and G the network shear modulus; and the permeo-elastic number $p \equiv \sigma_p/G$ with σ_p the permeation stress. Note that values of σ_p have not been reported in the literature, to the best of our knowledge; for this reason, we employ Eq. (E1) with typical values for surface tensions to get order-of-magnitude estimates of its range of variation. To this end, we substitute $\rho \approx r_f^2/\xi^2$, with r_f denoting the radius of the filaments constituting the network. Below, we consider three distinct systems, one synthetic, and two biological ones.

System I comprises the demixing of fluorinated oil embedded in a silicone gel, studied in great detail in Refs. [11–13]. The elastic modulus G is in the range $1.4 - 280$kPa (we employ a Poisson ratio $\nu = 0.5$ to convert from reported values of the Young's modulus). Following Ref. [12], we relate the modulus of this polymer network to its mesh size ξ through $\xi \sim (k_BT/G)^{1/3}$ with $k_BT = 4 \times 10^{-21}$J the thermal energy. Hence, $\xi \sim 2.4 - 14$nm. As for the surface tension, we employ $\gamma \approx 4.4\text{mN}\,\text{m}^{-1}$, as reported in Ref. [13]. We take a representative molecular radius $r_f \approx 0.2$nm

for PDMS chains, which yields $\sigma_p \sim 9 - 300$kPa (we emphasize that this is a rough estimate). The value $\alpha \approx 1.5$ (as the ratio between cavitation pressure and shear modulus) is reported in Ref. [11]. We conclude that the range of variation of dimensionless parameters h for system I is $h \sim 20 - 700 \gg \alpha$ and $p \sim 1.1 - 6.5 \gtrsim \alpha$, where larger values of h and p both correspond to softer gels. Our theory thus predicts that the relevant regime is predominantly cavitation (scenario i), with permeation (iii) being marginally possible for very stiff gels. This is consistent with the experimental observation of large, micron-sized droplets (while the mesh size is in the nanometer range) that fully exclude the surrounding network, as characterized by coherent anti-Stokes Raman scattering [13].

System III generally encompasses liquid condensates found in the nucleus of eukaryotic cells and mechanically interacting with the chromatin network, both native (such as nucleoli [14]) and biomimetic (such as CasDrop opto-genetically activated condensates [15]). Due to the broad class of systems considered and to the scarcity of available quantitative data for physical parameters, we report only conservative ranges for our estimates. Following Ref. [15], we estimate the elastic modulus to be in the range $G \sim 10 - 1000$Pa and a mesh size $\xi \sim 7 - 20$nm, with larger mesh sizes corresponding to softer chromatin. We estimate the surface tension to be in the range $\gamma \sim 10^{-7} - 10^{-6}\,\mathrm{N\,m^{-1}}$. Indeed, such low values of surface tension have been reported for nucleolar proteins, $\gamma \sim 4 \times 10^{-7}\,\mathrm{N\,m^{-1}}$ [14]. We take a radius $r_f = 1$nm for DNA, and a volume fraction $\rho \sim 0.1 - 0.4$ [15], which yields $\sigma_p \sim \pm 10 - 100$Pa (note that the sign of σ_p depends on whether the nucleoplasm or the liquid condensate better wets the chromatin, which is not known *a priori*). No value of α has been reported to our knowledge, and so we take $\alpha \sim 2.5$, corresponding to the neo-Hookean case, as a default. This results in a very broad range of possible values for dimensionless parameters, $h \sim 10^{-2} - 10$ and $p \sim \pm 10^{-2} - 10$. In particular, all three scenarios appear to be plausible: cavitation (i) in soft chromatin and for rather large values of the surface tension; nanodroplets confined at the mesh size (ii) if chromatin is stiffer and for low liquid-liquid surface tension; and finally permeation (iii) if the interfacial energy between chromatin and the condensate is low. Interestingly, only scenario *(i)* has been characterized yet: both nucleoli and engineered condensates form micron-sized droplets that have been shown to exclude the surrounding chromatin as they grow [15]. However, it is possible that mesh-size-level droplets actually exist, but have not been characterized yet as they would be significantly below optical resolution.

System II, finally, encompasses cytoplasmic liquid condensates such as stress granules and P-bodies, which interact mechanically with cytoskeletal networks, in particular the actin cortex. The main changes compared to system II are the properties of the elastic network. Reported values for the shear modulus of the cytoskeleton in intracellular conditions are similar in range to the nucleus, $G \sim 10 - 100$Pa [16]. However, the mesh size of the actin cortex, $\xi \sim 50 - 150$nm [17], is much larger than that of chromatin, as it is composed of sparser, stiffer filaments. We take a radius $r_f \sim 2.5$nm for F-actin filaments. Ref. [18] reports a surface tension $\gamma \approx 1\mu\mathrm{N\,m^{-1}}$ for cytoplasmic P-granules. The permeation stress is thus $\sigma_p \sim 0.2 - 2$Pa. The range for dimensionless parameters is thus $h \sim 0.2 - 6$ and $p \sim \pm 10^{-3} - 0.2$. Interestingly, this excludes cavitation (i): permeation (iii) is the predominant scenario, while microdroplets (ii) remain marginally possible. It is therefore an open question whether permeation actually occurs in experiments.

[1] S. Biwa, Cavitation in finite elasticity with surface energy effects, International Journal of Non-Linear Mechanics **41**, 1084 (2006).

[2] A. Meurer, C. P. Smith, M. Paprocki, O. Čertík, S. B. Kirpichev, M. Rocklin, A. Kumar, S. Ivanov, J. K. Moore, S. Singh, T. Rathnayake, S. Vig, B. E. Granger, R. P. Muller, F. Bonazzi, H. Gupta, S. Vats, F. Johansson, F. Pedregosa, M. J. Curry, A. R. Terrel, Š. Roučka, A. Saboo, I. Fernando, S. Kulal, R. Cimrman, and A. Scopatz, SymPy: symbolic computing in Python, PeerJ Computer Science **3**, e103 (2017).

[3] L. R. G. Treloar, *The Physics of Rubber Elasticity*, third edition ed., Oxford Classic Texts in the Physical Sciences (Oxford University Press, Oxford, New York, 2005).

[4] R. W. Ogden, *Non-linear Elastic Deformations* (Courier Corporation, 1997).

[5] C. O. Horgan and G. Saccomandi, A Molecular-Statistical Basis for the Gent Constitutive Model of Rubber Elasticity, Journal of Elasticity **68**, 167 (2002).

[6] A. N. Gent, A New Constitutive Relation for Rubber, Rubber Chemistry and Technology **69**, 59 (1996).

[7] E. M. Arruda and M. C. Boyce, A three-dimensional constitutive model for the large stretch behavior of rubber elastic materials, Journal of the Mechanics and Physics of Solids **41**, 389 (1993).

[8] M. C. Boyce, Direct Comparison of the Gent and the Arruda-Boyce Constitutive Models of Rubber Elasticity, Rubber Chemistry and Technology **69**, 781 (1996).

[9] P. Virtanen, R. Gommers, T. E. Oliphant, M. Haberland, T. Reddy, D. Cournapeau, E. Burovski, P. Peterson, W. Weckesser, J. Bright, S. J. van der Walt, M. Brett, J. Wilson, K. J. Millman, N. Mayorov, A. R. J. Nelson, E. Jones, R. Kern, E. Larson, C. J. Carey, İ. Polat, Y. Feng, E. W. Moore, J. VanderPlas, D. Laxalde, J. Perktold, R. Cimrman, I. Henriksen, E. A. Quintero, C. R. Harris, A. M. Archibald, A. H. Ribeiro, F. Pedregosa, and P. van Mulbregt, SciPy 1.0: fundamental algorithms for scientific computing in Python, Nature Methods **17**, 261 (2020).

[10] P. G. De Gennes, Liquid-liquid demixing inside a rigid network. Qualitative features, The Journal of Physical Chemistry **88**, 6469 (1984).
[11] R. W. Style, T. Sai, N. Fanelli, M. Ijavi, K. Smith-Mannschott, Q. Xu, L. A. Wilen, and E. R. Dufresne, Liquid-Liquid Phase Separation in an Elastic Network, Physical Review X **8**, 011028 (2018).
[12] K. A. Rosowski, T. Sai, E. Vidal-Henriquez, D. Zwicker, R. W. Style, and E. R. Dufresne, Elastic ripening and inhibition of liquid–liquid phase separation, Nature Physics **16**, 422 (2020).
[13] J. Y. Kim, Z. Liu, B. M. Weon, T. Cohen, C.-Y. Hui, E. R. Dufresne, and R. W. Style, Extreme cavity expansion in soft solids: Damage without fracture, Science Advances **6**, eaaz0418 (2020).
[14] M. Feric, N. Vaidya, T. S. Harmon, D. M. Mitrea, L. Zhu, T. M. Richardson, R. W. Kriwacki, R. V. Pappu, and C. P. Brangwynne, Coexisting liquid phases underlie nucleolar sub-compartments, Cell **165**, 1686 (2016).
[15] Y. Shin, Y.-C. Chang, D. S. W. Lee, J. Berry, D. W. Sanders, P. Ronceray, N. S. Wingreen, M. Haataja, and C. P. Brangwynne, Liquid Nuclear Condensates Mechanically Sense and Restructure the Genome, Cell **175**, 1481 (2018).
[16] A. F. Pegoraro, P. Janmey, and D. A. Weitz, Mechanical Properties of the Cytoskeleton and Cells, Cold Spring Harbor Perspectives in Biology **9**, a022038 (2017).
[17] T. Hohmann and F. Dehghani, The Cytoskeleton - A Complex Interacting Meshwork, Cells **8**, 10.3390/cells8040362 (2019).
[18] C. P. Brangwynne, C. R. Eckmann, D. S. Courson, A. Rybarska, C. Hoege, J. Gharakhani, F. Jülicher, and A. A. Hyman, Germline P Granules Are Liquid Droplets That Localize by Controlled Dissolution/Condensation, Science **324**, 1729 (2009).